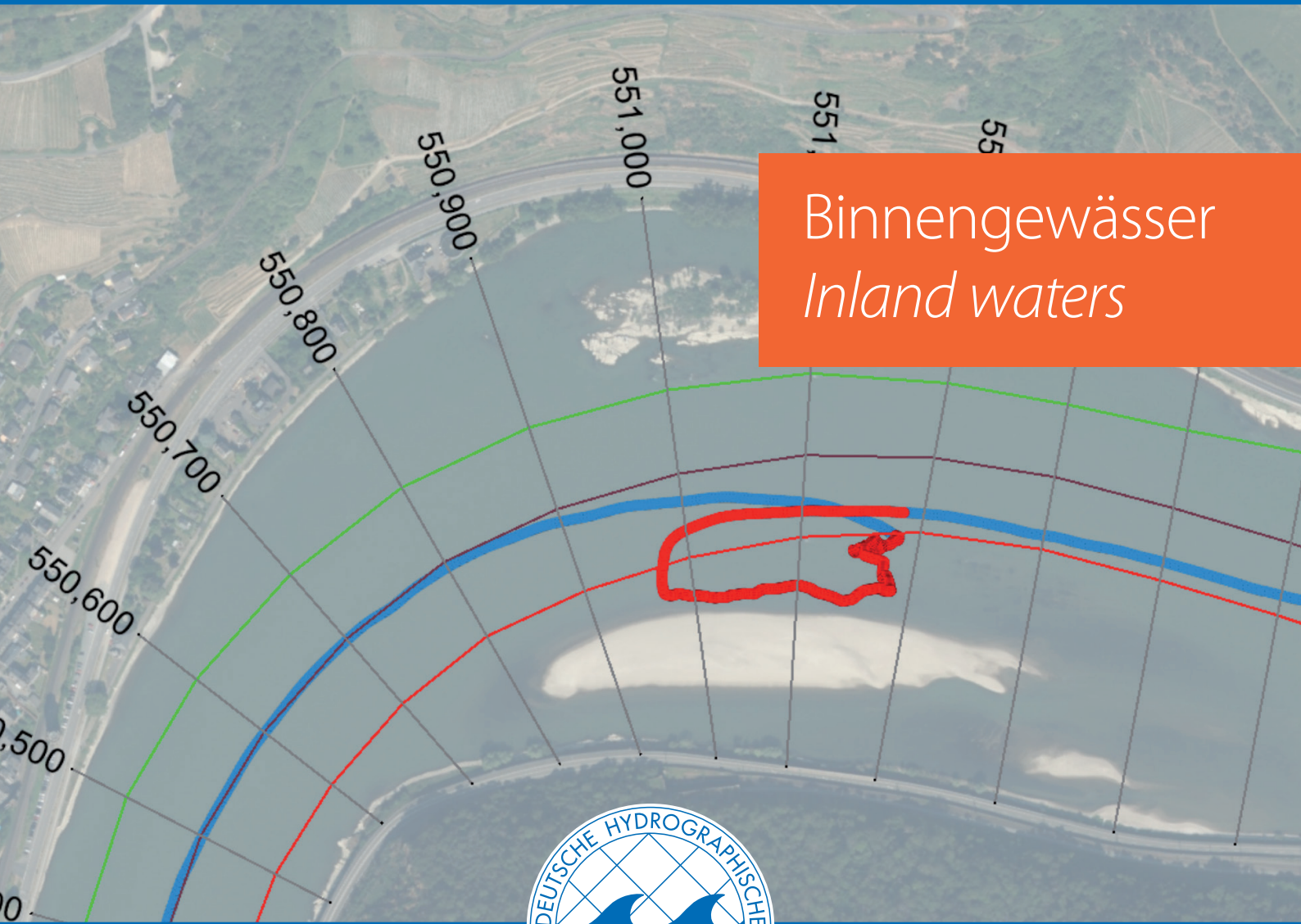


Journal of Applied Hydrography

HYDROGRAPHISCHE NACHRICHTEN

03/2025

HN 130



Binnengewässer
Inland waters



Mapping shallow inland running waters with UAV-borne photo and laser bathymetry

The Pielach River showcase

An article by GOTTFRIED MANDLBURGER, JAN RHOMBERG-KAUERT, LAURE-ANNE GUEGUEN, CHRISTIAN MULSOW, MARKUS BREZOVSKY, LUCAS DAMMERT, JOE HAINES, SILVIA GLAS, THERESA HIMMELSBACH, FREDERIK SCHULTE, PHILIPP AMON, LUKAS WINIWARTER, BORIS JUTZI and HANS-GERD MAAS

Mapping and monitoring of inland water bodies is of high scientific, economic and ecological importance. Depending on the size, depth and turbidity of the river, either acoustic or optical methods are suited for the acquisition of dense and accurate 3D bathymetry data. For relatively small, clear and shallow alpine rivers, optical methods are the first choice. Either images or laser scans are taken from crewed or uncrewed platforms to map the river bottom. For more than a decade, a near natural reach of the pre-alpine Pielach River in eastern Austria has been repeatedly surveyed with laser and photo bathymetry. In this contribution, we present an open benchmark dataset (DOI: 10.48436/taz19-r6618), which was captured in October 2024 following a devastating flood event in September 2024 with multicopter drones. We present the measurement campaign including airborne and terrestrial surveys and the data processing steps. Next to standard processing, we introduce new and innovative image-based bathymetry techniques for rivers with dynamic, wavy water surfaces. We show that image sequences can be used to mitigate the water surface dynamics; synchronous oblique drone images can be used to reconstruct the undulating water surface; and Neural Radiance Fields are an alternative option to classical methods for mapping bathymetry.

multimedia photogrammetry | topo-bathymetric laser scanning | water surface mapping | Neural Radiance Fields | full-waveform analysis | benchmark data
Multi-Medien-Photogrammetrie | topo-bathymetrisches Laserscanning | Wasseroberflächenkartierung | Neural Radiance Fields | Full-Waveform-Analyse | Benchmark-Daten

Die Kartierung und Überwachung von Binnengewässern ist von großer wissenschaftlicher, wirtschaftlicher und ökologischer Bedeutung. Je nach Größe, Tiefe und Trübung des Flusses eignen sich entweder akustische oder optische Methoden für die Erfassung dichter und genauer 3D-Bathymetriedaten. Für relativ kleine, klare und flache Alpenflüsse sind optische Methoden die erste Wahl. Von bemannten oder unbemannten Plattformen aus werden entweder Bilder oder Laserscans aufgenommen, um die Flusssohle zu kartieren. Seit mehr als einem Jahrzehnt wurde ein naturnaher Abschnitt der voralpinen Pielach in Ostösterreich wiederholt mit Laser- und Fotobathymetrie vermessen. In diesem Beitrag stellen wir einen offenen Benchmark-Datensatz vor (DOI: 10.48436/taz19-r6618), der im Oktober 2024 nach einem verheerenden Hochwasserereignis im September 2024 mit Multikopter-Drohnen aufgenommen wurde. Wir stellen die Messkampagne mit luftgestützten und terrestrischen Erhebungen sowie die Datenverarbeitungsschritte vor. Neben der Standardverarbeitung führen wir neue und innovative bildbasierte Bathymetrietechniken für Flüsse mit dynamischen, welligen Wasseroberflächen ein. Wir zeigen, dass Bildsequenzen verwendet werden können, um die Dynamik der Wasseroberfläche abzuschwächen; dass synchrone, schräge Drohnenbilder verwendet werden können, um die wellenförmige Wasseroberfläche zu rekonstruieren; und dass Neural Radiance Fields eine Alternative zu klassischen Methoden für die Kartierung der Bathymetrie darstellen.

1 Introduction

Precise 3D mapping of inland running water bodies is of high importance for flood risk modelling

(Tsakiris 2014), habitat mapping (Naura et al. 2016; Hauer et al. 2009), monitoring of fluvial erosion and sediment transport (Gkiatas et al. 2022; Kramer

Stajanko et al. 2023) and many other applications. This concerns both the shape of the underwater topography and submerged objects such as macrophytes (Rhombert-Kauert et al. 2024; Wagner et al. 2024) and deadwood (Zigann et al. 2023). Larger navigable rivers often show a substantial load of suspended sediment, making the water turbid. For those inland water bodies, Sound Navigation and Ranging (SONAR) based on single-beam or multibeam echo sounding is often the only option for acquiring 3D riverbed data (Lurton 2002). However, for moderately deep and clear alpine rivers, active and passive optical methods such as laser bathymetry (Philpot 2019; Guenther et al. 2000) and photo bathymetry (Mulsow et al. 2024; Maas 2015; Mandlbürger 2019) are often more applicable compared to SONAR-based data acquisition, because many small to medium-sized rivers are not continuously navigable for survey vessels and the application of small uncrewed surface vehicles is threaded by currents. However, the complex wavy water surface poses problems for both image- and laser-based surveys (Sardemann et al. 2024; Mulsow et al. 2024), especially when carried out by uncrewed aerial vehicles (UAV).

Although low flying altitudes enable high spatial resolution, with typical laser footprint diameters of less than a decimetre and image ground sampling distances even in the centimetre range, the higher resolution also comes with the downside of a higher sensitivity with respect to local water surface inclination. For photo bathymetry, this complicates the derivation of underwater tie points (Gueguen and Mandlbürger 2024), which are necessary for image orientation in the multi-media case (Mulsow 2010), and later also the derivation of dense underwater point clouds (Mandlbürger 2019). Laser bathymetry is less sensitive in this respect, as green laser pulses are also reflected to a certain extent from the water surface (Guenther et al. 2000) and, in the best case, provide both surface and bottom information for a single emitted laser pulse. But also for laser bathymetry, the higher resolution increases the chance that the collimated laser pulses entirely hit the side of a water wavefront facing away from the sensor, which results in water surface dropouts. Another problem for laser bathymetry is the very shallow zone, where the reflected echo pulse can no longer be separated into distinct returns from the surface and the bottom (Schwarz et al. 2019). Thus, water surface modelling is not straightforward, but requires expert intervention to some extent. Practical workflows for photo and laser bathymetry therefore often rely on simplified water surface models neglecting the dynamic, wavy water surface. This decreases precision and accuracy (Westfeld et al. 2017) and makes image-based derivation of bottom topography impossible, especially for deeper areas.

From the above, we can conclude that both laser and photo bathymetry would benefit from (i) better methods for coping with dynamic, wave-induced water surface and (ii) existence of trustworthy ground-truth reference data to validate new and innovative data processing strategies. The aim of this contribution is therefore to introduce a real-world benchmark reference dataset, openly accessible to the scientific community, and to introduce new ideas and concepts for deriving precise bathymetry based on aerial images and laser scans. As a basis, we organised a multi-purpose and multi-sensor measurement campaign at the pre-alpine Pielach River in October 2024 following a major flood event in September 2024 (Bloeschl 2024). In the contribution, we first describe the study area and the captured datasets in Section 2. In Section 3 we provide detailed information on how the acquired measurements were post-processed to ensure a reliable benchmark dataset. This includes detailed descriptions of the processing of the topo-bathymetric UAV-laser scanning mission, and the UAV-based acquisition of oblique and aerial images. In this Section, we also introduce innovative concepts for deriving bathymetry from (stereo) images, using conventional or deep learning-based approaches. We present the resulting benchmark dataset including representative error metrics in Section 4. In the same Section, we also briefly show the first results of the advanced photo bathymetry methods, and we briefly discuss the obtained results. The article is summarised by the concluding remarks in Section 5.

2 Materials

2.1 Study area

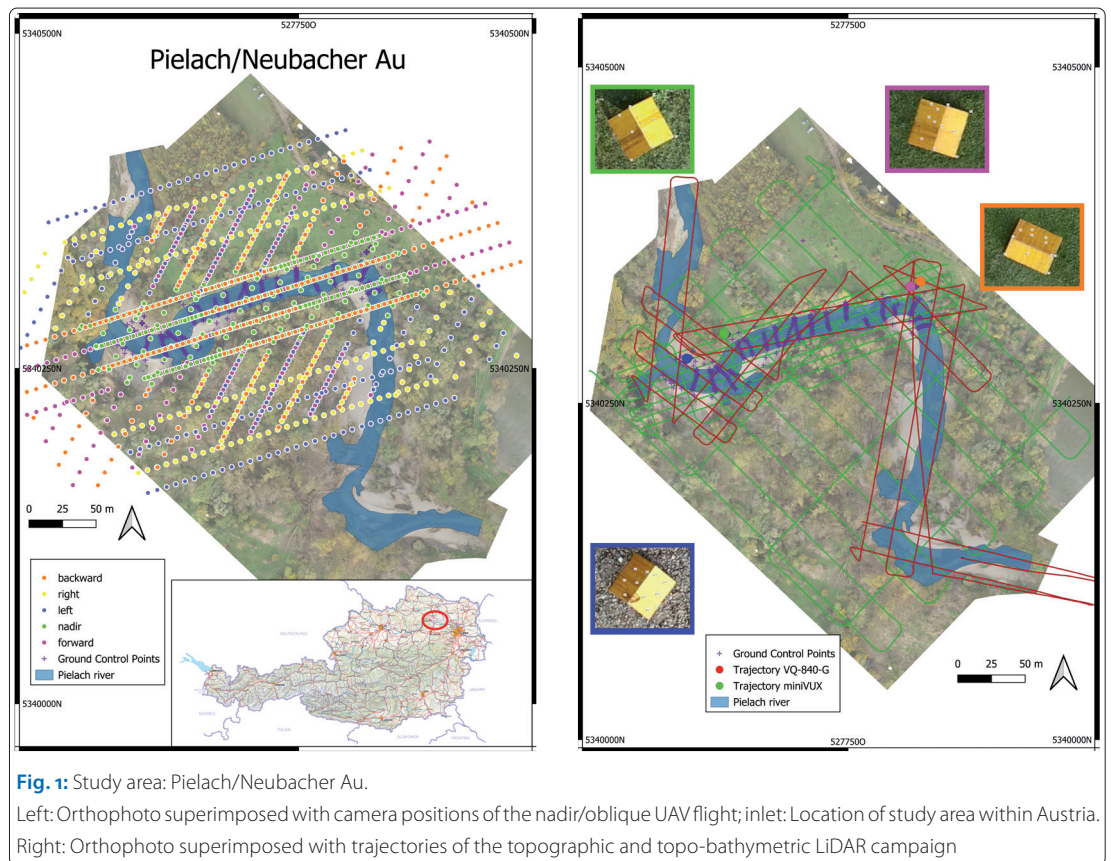
The study area Neubacher Au (N 48°12'50", E 15°22'30"; WGS 84) is located in eastern Austria in the tailwater of the pre-alpine Pielach River, a right-hand side tributary of the Danube (see Fig. 1). The study area is located within a natural conservation area of the European Union Natura2000 programme (area code: AT1219000). In the southern part of the study reach, a complete meander loop of the river encloses a riparian forest. North of the river, there is a pasture. The morphology is dominated by gravel banks, point bars and steep cliffs. The river is classified as a riffle-pool type (Melcher and Schmutz 2010), reaching a maximum depth of about 3 m. It is characterised by a pluvio-nival regime with typical discharge peaks during the winter/spring snow melt and heavy rainfall in the summer. However, the last flood event in September 2024 was caused by perpetual precipitation over a period of more than four days (Bloeschl 2024).

The mean annual discharge within the investigated area is about $7 \text{ m}^3 \text{ s}^{-1}$, the sediment of the bed load is dominated by coarse gravel (2 cm to 6.3 cm), and the average gradient is about 0.4 %.

Authors

Prof. Gottfried Mandlbürger, Jan Rhombert-Kauert, Laure-Anne Gueguen, Markus Brezovsky and Lucas Dammert work at TU Wien, Austria. Christian Mulsow and Prof. Hans-Gerd Maas work at TU Dresden, Germany. Joe Haines works at Newcastle University, UK. Silvia Glas, Theresa Himmelsbach, Frederik Schulte and Prof. Lukas Winiwarter work at the University of Innsbruck, Austria. Philipp Amon works at RIEGL Research Forschungsgesellschaft mbH in Horn, Austria. Prof. Boris Jutzi works at the Karlsruhe Institute of Technology, Germany.

gottfried.mandlbuerger@geo.tuwien.ac.at



The entire catchment area of the Pielach River measures 590 km² and the mean channel width is approximately 20 m. Although the longitudinal continuum of the Pielach River is disrupted by weirs built for hydropower use and engineering measures, the river has retained some of its natural self-forming morphological characteristics, such as periodically inundated sidearms, dynamic gravel bars, large woody debris, small oxbows, etc., within the study area (Zitek et al. 2008). A more detailed description of the study area and its surrounding can be found in Mandlbürger et al. (2015).

2.2 Datasets

To obtain data to tackle the research questions formulated in Section 1, a multi-purpose measurement campaign was conducted on October 24 and 25, 2024. The campaign was carried out one month after the severe flood event on September 20 and 21, 2024. By then, the river had regained a good level of transparency, which, in turn, enabled optimal conditions for optical hydrography.

As advancements in photo bathymetry are the main motivations of the entire initiative, we conducted multiple UAV image acquisitions. First, the straight east-west river section was captured with nadir and oblique images using a DJI Zenmuse P1 45 MPix RGB-camera mounted on a DJI M350 RTK multicopter UAV. With a flying altitude of 80 m above ground level (AGL), the resulting ground sampling distance (GSD) amounts to 1 cm for the

nadir images. The oblique images were taken with an angle of 45° using the smart oblique mode in the DJI Pilot 2 flight controller app, which means that the gimbal constantly swings forward, backward and sideward to mimic a classical penta camera with a Swiss-cross pattern. The left panel of Fig. 1 shows the positions and orientations of the cameras. This flight block specifically served for the comparison of classical Dense Image Matching (DIM) versus photo bathymetry based on Neural Radiance Fields (NeRF) (Mildenhall et al. 2021).

To test the possibility of improving photo bathymetry in the presence of waves with image sequences, we performed a second image acquisition, where the UAV stopped at predefined waypoints and hovered in the air for about 1 minute while images were taken with a frame rate of 0.7 Hz. This results in sequences of about the 100 images per waypoint before the UAV was flying to the next waypoint, where the same procedure was repeated. Adjacent image sequences had an overlap to enable 3D stereo reconstruction. In this experiment, we tested flying altitudes of 25 m, 50 m and 75 m, respectively, generating GSDs of 3 mm to 9 mm.

Finally, this measurement campaign was our first opportunity to obtain a field dataset to map the undulating water surface with oblique and synchronously captured stereo images, after working only with laboratory data (Gueguen and Mandlbürger 2024). The goal was to apply our processing

workflow to field data and understand their subsequent specificity. In order to highlight an optimal configuration, we acquired data from four different positions and imaging directions with respect to the river flow direction. For that, we used two DJI M350 drones, each equipped with a DJI Zenmuse P1 camera. The two drones were manually controlled so that pairs of oblique images were taken at each point. The UAVs hovered at these manually defined positions and took oblique images with a frame rate of 1 Hz. At this stage of the project, the synchronisation of the image capture was only done manually, with both drone pilots triggering image sequence capture at an acoustic signal. We also took care that as many ground control points (GCP) as possible are visible in both images to allow image orientation via spatial resection for each pair of images.

To provide proper reference for the aforementioned photo bathymetry experiments, we conducted UAV laser scanning flights with both topographic and topo-bathymetric UAV laser scanners. We first captured the entire study area including the alluvial forest with a RIEGL miniVUX-3UAV laser scanner operating a near-infrared (NIR) laser with a wavelength of 905 nm and a pulse repetition frequency of 300 kHz. The sensor is equipped with a RiLOC-E navigation unit, consisting of a helix GNSS antenna, a u-blox dual-band GNSS receiver and a MEMS IMU. For colourising the resulting 3D point cloud, the sensor is equipped with a Sony $\alpha 6000$ RGB camera. We flew the system 60 m AGL with a flight speed of 6 m s^{-1} . These mission settings resulted in a point density of more than 500 points/m². The flight trajectory is shown in Fig. 1. Data processing was carried out in the scanner manufacturer's software RiPROCESS using Online WaveForm Processing (OWP) (Pfennigbauer et al. 2014). From this dataset, we derived a digital terrain model (DTM) of the dry area and a digital water surface model (DWSM), which we later used for refraction correction.

To obtain continuous underwater data, we conducted a topo-bathymetric UAV survey with the RIEGL VQ-840-GL laser scanner. The sensor uses a green water penetrating laser operating at a wavelength of 532 nm. The scanner features an elliptical Palmer scan mechanism with a lateral Field of View (FoV) of $\pm 20^\circ$ and a forward/backward FoV of $\pm 14^\circ$. We flew the sensor at a flying altitude of 60 m AGL with pairs of flight lines aligned to the river axis and additional cross-strips in the area of specific interest in the northwestern part of the study area as plotted in the right panel of Fig. 1. As with the NIR laser, RiPROCESS was also used to process the green laser data. Waveform analysis was carried out using the standard OWP approach and the water-specific Surface-Volume-Bottom (SVB) algorithm (Schwarz et al. 2019). Due to the good water

System	Flight altitude	Beam divergence	Pulse repetition rate
RIEGL VQ-840-GL	60 m \pm 5 m	1 mrad	199 kHz
RIEGL miniVUX-3UAV	60 m \pm 14 m	1,5 mrad	300 kHz

Table 1: The different settings and parameters of the LiDAR systems used in the survey

clarity, we were able to capture the entire riverbed, including the approximately 3 m deep pool areas (cf. Fig. 4). Table 1 summarises the parameters used for both LiDAR surveys.

In addition to the LiDAR point clouds shown in Fig. 4, the RIEGL VQ-840-GL is able to capture full-waveform data (Fig. 2). This feature enables the processing using the SVB algorithm, as here a possible decomposition is fitted to the waveform data, requiring an extended record of the reflected laser pulse.

To allow accurate georeferencing and evaluation of the geometric quality of the acquired datasets, a geodetic reference network was established in the study area. Four static GNSS position observations constitute the basis of the network (Fig. 3). The points were observed between 1.5 and 5.5 hours. For post-processing of these long-term GNSS measurements, we used a local base station in the nearby village of Loosdorf, which led to baselines shorter than 2 km. These four points define the datum of the local realisation of ETRS89 (reference epoch: 2015.0, UTM 33N, EPSG: 25833).

The inner geometry of the network is defined by total station measurements from four positions, of which two are identical with the GNSS points. A Leica MS60 robotic total station was used and the local coordinate uncertainties of the fixed network points reach 2 mm in position and 3 mm in height after adjustment. Transformation into a global ETRS89/UTM 33 coordinate system yielded an uncertainty of less than 5 mm. Based on the total station network, we measured photogrammetric targets above and below the water surface, as well as bathymetric cross-sections (cf. Fig. 3). These measurements were not included in the network adjustment to allow maximum accuracy of the inner

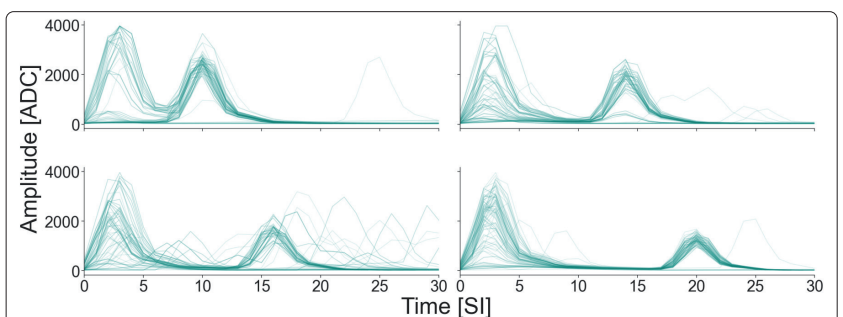


Fig. 2: Full-waveform data of the cross-section shown in Fig. 4 for the green LiDAR system. Each panel displays 100 recorded waveforms for different depths of the cross-section, where one sample interval equals approximately 0,5 ns and the amplitude is given in units of the system's Analog-to-Digital Converter (ADC)

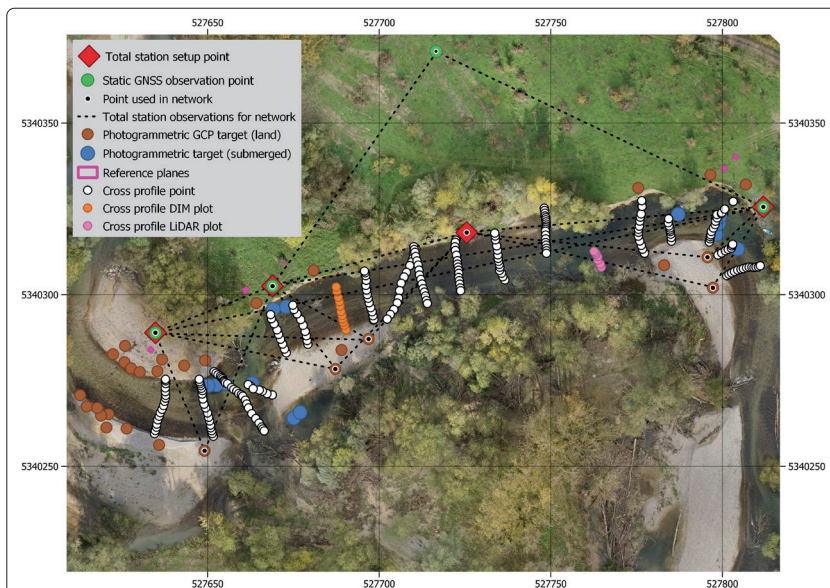


Fig. 3: Overview of the network of reference measurements. The geodetic datum (ETRS89/UTM 33) is defined by the four GNSS points (green). All photogrammetric ground control points (brown) and river cross-sections (white) were measured from total station network points (red diamond). The river cross-sections marked with blue and orange points are shown in Fig. 4 and Fig. 9C, respectively

geometry of the measurements. While the above-water photogrammetric targets were measured using an accurate mini reflector, the profiles and below-water targets were measured with a pole and a 360° prism. In addition to the inherent deviations of 360° prisms (about 3 mm), the long pole 1.8 m introduces an additional uncertainty because pole levelling proved difficult in the strong currents of the Pielach River. To increase accuracy, we repeatedly measured the underwater targets and averaged the measurements. To counteract the effect of the submersion of the pole tip in the river sediment, a special pole adapter was used for bathymetric measurements. The adapter is a disk with a diameter of 6 cm instead of a classic tip at the bottom of the prism pole. However, the effect

of the pole tip submersion is presumably still larger than the uncertainty introduced by the slight inclination of the prism pole and the prism deviations. Our assessment of the uncertainty of the measurement shows that, e.g., the bathymetric profiles exhibit a global uncertainty of less than 18 mm for the data in ETRS89/UTM 33N and a local uncertainty of only 13 mm towards our local realisation of the geodetic network.

The georeferencing for the LiDAR data is established using eight sloped planes (saddle roofs) set up in the study area (Fig. 1 and Fig. 3). Similarly to the photogrammetric targets used for georeferencing the photogrammetric bundle block adjustment, the eight planes are used to transform the strip-adjusted LiDAR data into our local coordinate system realisation. Our investigation shows that a shift of $(-2.2, 1.9, 3.6)^T$ cm was necessary for the miniVUX-3UAV data and of $(-1.2, 1.4, -11.7)^T$ cm for the VQ-840-GL data to transform the data into the coordinate system defined by the terrestrial network. With the exception of the rather high vertical correction necessary for the VQ-840-GL dataset, these values lie exactly in the expected uncertainty range of the GNSS-RTK georeferenced airborne LiDAR datasets.

3 Methods

In this Section, we briefly describe the data processing methods employed. We first focus on a description of the general photogrammetric and LiDAR workflows used to convert the raw laser and image data to georeferenced and refraction-corrected 3D point clouds (Sections 3.1 and 3.2). Later, we also describe details of the three conducted experiments, namely deriving bathymetry from stereo image sequences (Section 3.3), mapping the water surface with oblique stereo images (Section 3.4), and reconstructing both topography and bathymetry with NeRFs (Section 3.5).

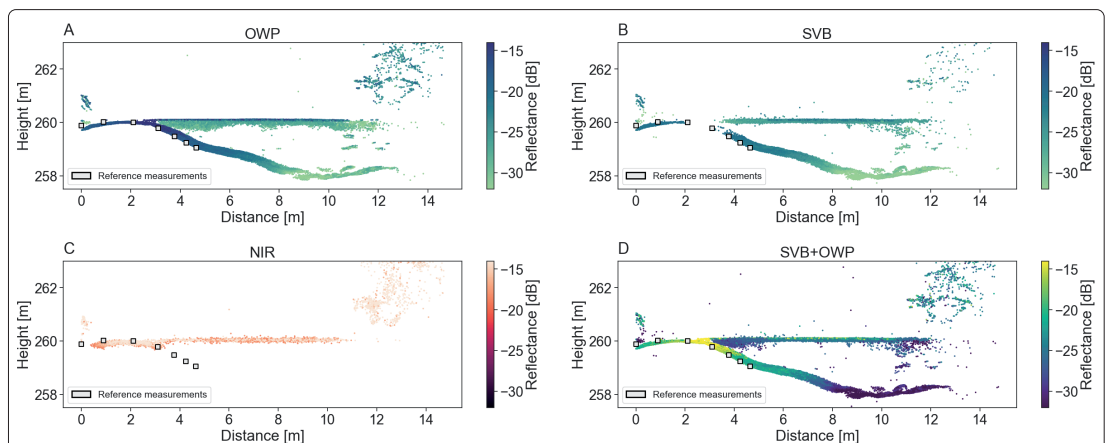


Fig. 4: Cross-section of a deeper section of the Pielach River. The different panels show the four types of point cloud data available in this study, near-infrared LiDAR (NIR) together with the green LiDAR processed using online waveform processing (OWP) and the surface-volume-bottom algorithm (SVB)

3.1 LiDAR workflow

The full waveforms of the topo-bathymetric LiDAR sensor introduced in Section 2.2 were processed by two different algorithms. While Online Waveform Processing (OWP) (Pfennigbauer et al. 2014) uses a reduced set of the recorded waveforms around signal peaks to extract points online during flight, the SVB algorithm (Schwarz et al. 2019) is applied in post-processing and aims to extract further data through the application of exponential decomposition (Schwarz et al. 2017) associated with the water column backscattering. This well-known physical foundation for the interaction of laser pulses with the water column improves the water surface detection and furthermore is able to capture deeper points than standard methods. The new points in this method can then furthermore be extended by the points produced during standard processing (OWP), enhancing the point cloud in turbid or deep waters. In contrast to that, only OWP was used to process the waveform data of the topographic data (miniVUX-3UAV).

Georeferencing and strip adjustment were performed using the method of Glira et al. (2016) implemented in the scientific laser scanning software OPALS (Pfeifer et al. 2014) for the topo-bathymetric LiDAR dataset and the holistic approach of Pöpll et al. (2024) integrated in RiPROCESS for the topographic LiDAR dataset. In both cases, the saddle roof reference surfaces (cf. Fig. 1) were used for precise georeferencing of the point cloud with respect to the ETRS89 system defined by the terrestrial reference network.

After full-waveform analysis and strip adjustment, refraction correction was performed for all underwater points of the resulting georeferenced 3D point cloud. The steps include (i) the derivation of a gridded water surface model, (ii) the calculation of beam vectors for each laser point (based on the trajectory) and (iii) the final run-time and refraction correction (Mandlbürger et al. 2015) implemented in the module Snellius of the OPALS software. The water surface model was obtained from the water surface reflections of the NIR laser data. Although the coverage with water surface points was not continuous, any gaps could be filled by interpolation.

3.2 Photogrammetric workflow

The block of nadir and oblique images shown in Fig. 1 was processed using a standard Structure-from-Motion (SfM) workflow. The procedure consists of finding image features in individual images, matching the features to obtain 3D tie points, and establishing the relative orientation for all overlapping image pairs. Georeferencing of the entire image block is done in a final step by first semi-automatically measuring the GCPs in the images and then performing the bundle block adjustment

(Förstner and Wrobel 2016; Kraus 2007) including on-the-job camera calibration based on all available data (tie points, GCPs). This provides the interior orientation of the employed DJI Zenmuse P1 camera (principal point, focal length, lens distortion parameters) and the exterior orientations of all captured images (XYZ coordinates of the projection centres, Omega/Phi/Kappa rotations angles). This is the basis for follow-up processing steps like creating a 3D point cloud via Dense Image Matching, as well as orthophoto and 3D mesh generation. The described procedure was carried out for both the nadir/oblique Zenmuse P1 images and also for the Sony $\alpha 6000$ images of the miniVUX-3UAV LiDAR survey.

As long as underwater features are visible in the images, a dense reconstruction of the topography of the river bottom is possible by first applying standard DIM (Wenzel et al. 2013; Hirschmüller 2008). The raw 3D DIM point cloud is too shallow if ray bending at the water surface is not considered. Refraction correction is achieved by connecting the raw DIM points with the projection centre of the images, from which the point was originally matched. The connecting lines constitute the image rays, which can be intersected with the water surface model, yielding the 3D position where the image ray enters the water column. Based on Snell's law of refraction, the direction of the underwater ray can be calculated (Bryant 1958). This procedure is repeated for each image ray of a raw 3D point, and then forward intersection is performed for all underwater rays, producing the refraction-corrected 3D position (Mandlbürger 2019). The described correction procedure is implemented in the OPALS software (Pfeifer et al. 2014). A comparable approach is described in Mulsow (2018).

3.3 Bathymetry from image sequences

As described in Section 1, the aim of this experiment is to integrate multiple images of a sequence showing the same scene and to mitigate the effect of the dynamic, wavy water surface. During the campaign, several image sequences were acquired from the hovering UAV. In order to obtain the maximum resolution, the camera was operated in frame image mode rather than video mode. The DJI Zenmuse P1 camera used can capture image sequences in full resolution with a frame rate of 0.7 Hz. For each spot, around 100 images were taken with activated motion compensation via the gimbal. However, the images were slightly moving by up to 30 pixels in every direction within a sequence.

The first step in the processing pipeline is therefore aligning or co-registering all images to a single reference frame in the middle of the sequence based on stable features on the river banks. This is necessary because of the (minor) instability of

the hovering UAV during image sequence acquisition. For that, stable tie points along the river banks were defined in the reference image. In order to suppress perspective and projective effects on co-registration, only points close to the water level were chosen. The number of tie points ranges from 20 to 40 points while a minimum of four points is required. Tie points were tracked and measured via Least Squares Matching (LSM) in all images of the sequence with sub-pixel precision. All images of a sequence were then aligned with the reference image by applying the best-fitting projective transformation. In our case, the inner accuracy ranges from 0.05 to 0.2 pixel.

All co-registered images of a sequence were stacked and handed over for final processing. The variation of grey values in each pixel position of the sequence is statistically analysed to find the representative grey value, which is not affected by the water surface dynamics. So far, empirical evidence has shown that median filtering is the most effective method to achieve optimal contrast and robustness in the resulting image (Mulsow et al. 2024). Thus, the standard strategy is to apply a median filter to the stacked grey values of each pixel position of the sequence. Values of 255 (overexposure) are excluded from the median filtering. For pixels showing mainly overexposed values, the algorithm has to be adapted. In that case, for example, the Minstore value (smallest pixel value) can be taken for the corrected image. If only fully saturated values of 255 were captured for one pixel position, the corrected value was interpolated from neighbouring pixels. The procedure is then repeated for all images of all individual sequences. Pairs of integrated stereo-images can then be used as basis for 3D bathymetry reconstruction using standard multi-media photogrammetry pipelines.

3.4 Water surface from oblique stereo images

The main processing direction is a standard SfM workflow and is performed pairwise with Agisoft Metashape. The steps are: (i) feature detection on each image and feature matching between both images, (ii) alignment of the cameras, (iii) georeferencing using the GCPs and finally (iv) dense matching. Highly textured and sharp features are required for efficient feature detection and matching, and since (i) water does not fit these criteria (due to specular reflection at the water surface), and (ii) our previous studies with lab data have shown the difficulty of using such a method on water bodies, we are also using deep learning-based solutions. In particular, we are interested in feature detection and feature matching, for example using Superpoint (DeTone et al. 2018) and LightGlue (Lindenberger et al. 2023), which have been shown to provide much higher quantities of valid match-

es for various datasets with low texture such as indoor environments. For this, we use the Hierarchical Localization toolbox hloc (Sarlin et al. 2019), which implements both. A benefit of this toolbox is that it also provides formats that are compatible with Metashape via Colmap, which means that the tie points and the 3D model resulting from Colmap can be imported into Metashape. Further analysis and processing can then be performed, such as outlier removal, scaling or georeferencing of the model and camera alignment optimisation.

3.5 Topography and bathymetry from NeRFs

Neural Radiance Fields (NeRFs) were first introduced in March 2020 (Mildenhall et al. 2021). Since then, they gained widespread attention and adoption. NeRFs enable the synthesis of novel scene views by optimising a continuous volumetric scene function using a given set of images. A NeRF represents a scene through a fully connected deep neural network based on 5D coordinates (spatial location and a viewing direction) as input, and outputs the volume density and view-dependent emitted radiance at that point.

The original NeRF algorithm is agnostic with respect to media changes, but different extensions considering ray refraction have been proposed in the recent past. Our own concept of dealing with underwater ray refraction for NeRF-based processing based on UAV images (i.e., through-water close-range bathymetry) is to train separate NeRFs for above and below the water surface assuming a simple, planar water surface as a starting point. Concepts for further adaptations include the consideration of slope variations on top of the simple water surface to compensate for wave effects or even to consider continuous refraction or at least discrete media changes along the image ray.

For the Pielach image dataset, we generated the NeRF using the Nerfstudio framework, which provides a simple API to streamline the end-to-end process of creating, training and testing NeRFs. The camera orientations form the basis for the creation of the NeRF. In Nerfstudio, we used the Nerfacto model, specifically the Nerfacto-Huge variant. This method required approximately 24 GB of GPU VRAM, which was available on our NVIDIA A40 graphics card.

4 Results and discussions

In this Section, we present and briefly discuss the results of the data processing outlined in Section 3. We first present the topo-bathymetric LiDAR data (Section 4.1) that constitute the reference for the benchmark dataset. Thereafter, we present the results of the classical and advanced techniques for mapping bathymetry and water surfaces in Sections 4.2 to 4.5.

4.1 LiDAR data

Fig. 5A shows a hill shading of the final topo-bathymetric DTM superimposed with a colour-coded depth map for a subset in the northwestern region of the study area. The depth map confirms the river structure as riffle-pool type with predominantly shallow water depths of less than 1 m and occasional deeper pools of up to 2.5 m. This is also quantitatively demonstrated in the water depth histogram shown in Fig. 5B.

To evaluate the topographic and topo-bathymetric laser scanning data, each LiDAR point cloud is compared to the different types of terrestrially measured targets. Here both the absolute vertical distance to the nearest neighbour of the references was calculated, as well as a normal plane distance based on the ten closest neighbours of the reference. For the references acquired shown in Fig. 3, both types of LiDAR data can be compared to checkerboard GCP targets and saddle roofs. For the NIR point cloud, the deviations between the LiDAR points and the GCP are mainly smaller than 2 cm for the vertical and normal distances. The discrepancies for saddle roofs are comparable with occasionally larger offsets due to rounding effects on the ridge line of both planes (Fig. 6).

For the green LiDAR point cloud, we evaluated the above- and below-water targets (GCPs, saddle roofs, submerged checkerboard targets, and riverbed points) for the three different processing methods (OWP, SVB and a combination of OWP and SVB). The results are shown in Fig. 7. There, a slightly lower accuracy can be observed, which might result from the larger laser footprint size of the bathymetric sensor. Larger deviations are observed for the SVB on the land targets (GCPs and saddle roofs), because the algorithm is tailored for bathymetric waveforms. Therefore, SVB land points can be considered outliers and thus do not reflect the representative measurement accuracy of the topo-bathymetric system. For all underwater targets, the accuracy is around ± 3 cm as can be seen in Fig. 7C.

Lastly, we assessed the underwater accuracy in more detail by comparing the transects measured with the total station and the underwater LiDAR point cloud. For all three methods, a similar absolute vertical distance can be seen in Fig. 8A. For the normal plane distance, the combined OWP and SVB + OWP data show similar distributions, only SVB shows slightly wider distributions, translating to slightly higher uncertainties (Fig. 8B).

We can conclude that, with respect to the residual deviations between the underwater LiDAR points and the terrestrially measured riverbed ground truth, the bathymetric LiDAR dataset adheres to the Exclusive Order, the most rigorous standard issued by the International Hydrographic

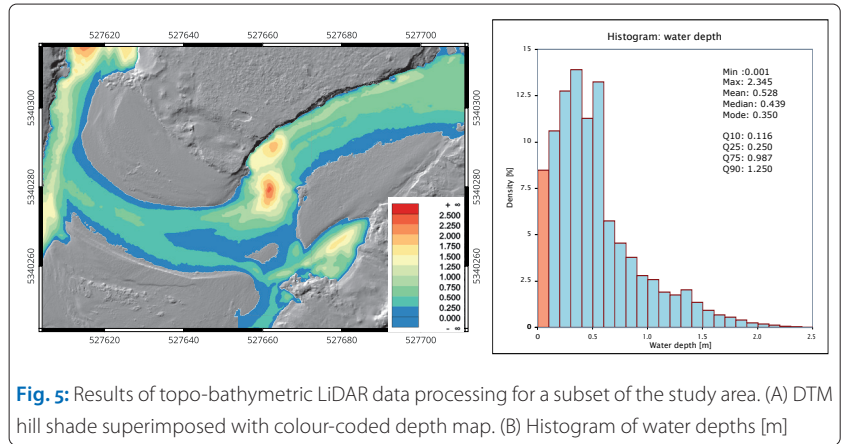


Fig. 5: Results of topo-bathymetric LiDAR data processing for a subset of the study area. (A) DTM hill shade superimposed with colour-coded depth map. (B) Histogram of water depths [m]

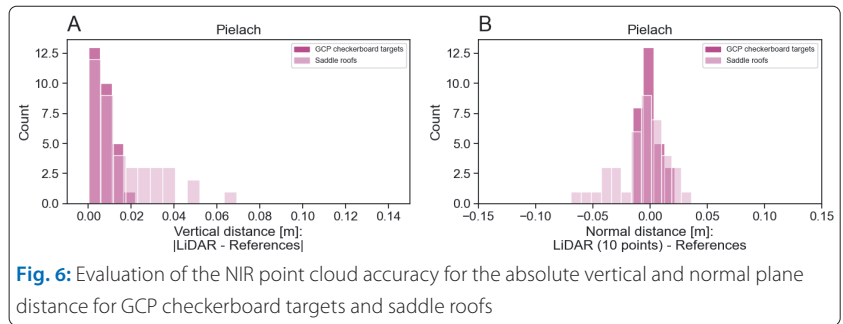


Fig. 6: Evaluation of the NIR point cloud accuracy for the absolute vertical and normal plane distance for GCP checkerboard targets and saddle roofs

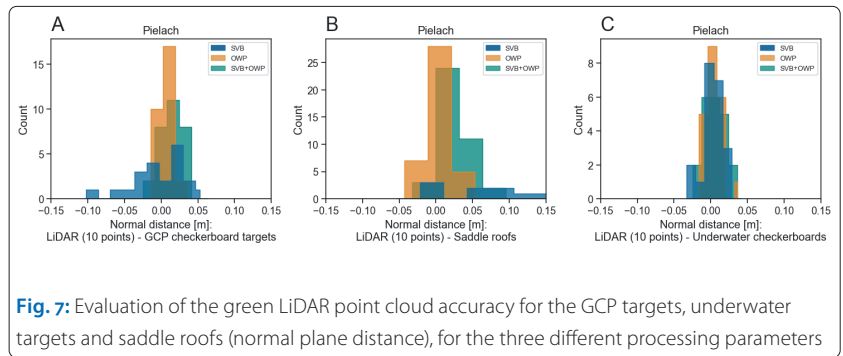


Fig. 7: Evaluation of the green LiDAR point cloud accuracy for the GCP targets, underwater targets and saddle roofs (normal plane distance), for the three different processing parameters

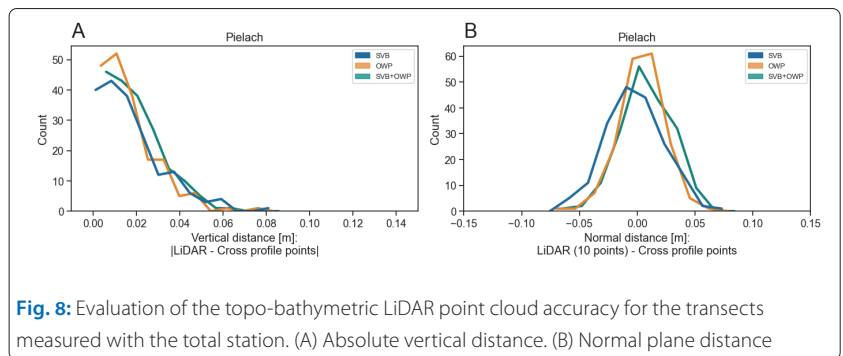
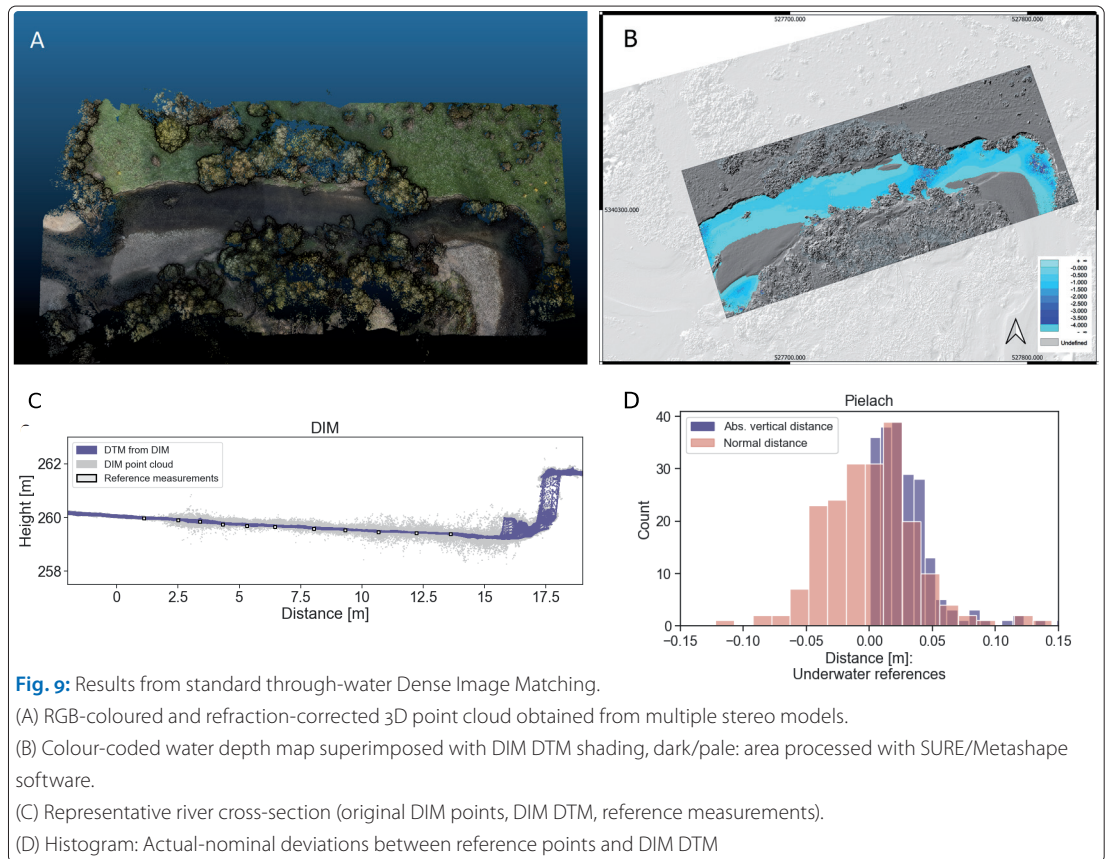


Fig. 8: Evaluation of the topo-bathymetric LiDAR point cloud accuracy for the transects measured with the total station. (A) Absolute vertical distance. (B) Normal plane distance

Organization (IHO 2008). The deviation between the riverbed reference points and the corresponding bathymetric LiDAR points is $0.5 \text{ cm} \pm 2 \text{ cm}$.

4.2 Bathymetry from standard through-water DIM

The results of the standard through-water photo bathymetry pipeline detailed in Section 3.2 are illustrated in Fig. 9. For a relatively shallow section



of the Pielach River, Fig. 9A and B show the 3D RGB point cloud corrected for refraction obtained from DIM and the hill shading of a DTM derived from DIM points by median filtering. Superimposed on the shading, Fig. 9B displays a colour-coded water depth map, which reveals depths of 0 m to 2 m. It can be clearly seen that the DIM-derived riverbed is smooth and consistent up to a water depth of up to 1.5 m, but becomes more noisy in deeper areas. The latter is visible in the deep pool in the north-west part of the scene. Here, image blurring and the associated loss of texture limit the achievable penetration depth of photo bathymetry.

For a representative transect, the DIM point cloud corrected for refraction, the final underwater DTM, and the terrestrially measured reference points are plotted in Fig. 9C. The point cloud (grey points) shows substantial spread underwater because of the shortcomings when not considering the dynamic, wavy water surface. However, for the shallow cross-section shown (max depth: approximately 1 m), the averaged DTM (violet) closely matches the underwater reference points (black/light grey) measured with the total station. The histogram shown in Fig. 9D confirms the good agreement between the underwater DTM derived from the UAV images and the reference points with vertical deviations mainly less than 5 cm. For all underwater reference points, the deviations (normal distances) with respect to the DIM-derived DTM measure $0 \text{ cm} \pm 4 \text{ cm}$. In other

words, the underwater DTM is unbiased with an RMSE of 4 cm.

4.3 Bathymetry from image sequences

For the Pielach dataset, the method described in Section 3.3 worked well, and the corrected image corresponds to an image that would have been taken through a calm flat water surface. Fig. 10 shows the results for the image sequence of a single spot. Fig. 10A displays the reference image, that is, the raw image taken from the middle of the entire sequence. All other images are co-registered to the reference image based on tie points in the dry or very shallow zone, which are tracked in all images of the sequence. The reference image and an arbitrary second image from the sequence are displayed in Fig. 10B together with the displacement vectors, which transform the moving image (cyan) to the reference image (red). After applying the transformation, the residual deviations in x/y are small with an RMSE of 0.11/0.10 pixel.

The final median filtered image of the sequence is plotted in Fig. 10C. Compared to the original (reference) image, the filtered image appears much smoother, clearer and sharper in the river area. The effectiveness of the procedure can best be judged from the small inlet images showing the submerged checkerboard targets. In the original (reference) image, the targets are blurred, and they regained their actual sharp black-white edges and sharp geometric features in the filtered image. In

future work, we will use these images for improved underwater stereo matching.

4.4 Water surface from oblique stereo images

Of the 2,165 pairs of images taken from different viewpoints, only 973 could be aligned with Agisoft Metashape and 1,487 with hloc. In addition, no tie point was detected on the water surface with Agisoft Metashape while hloc had for most pairs around 80 tie points on the water surface, which already shows a clear difference of performance between these tools. As an example, Fig. 11 shows the results of the feature matching using hloc for pair 583. In this case, we can see 71 tie points that were found on the water surface. To assess the accuracy of the water surface tie points detected by deep learning, we used the digital water surface model as a reference. The following are the results presented for pair 583, but the same observations were made for other examples. Since the GCPs are non-coded targets, the comparison of the tie points with the DEM is not a step that is automatised in the processing workflow, hence we cannot provide global results.

After importing the tie point cloud from hloc in Agisoft Metashape and georeferencing it into our coordinate system, the orientation of the images is estimated via bundle block adjustment. In this case, the re-projection error was around three pixels. In order to obtain a better accuracy, we have selected three images in addition to our selected pair to add redundancy to the bundle block adjustment. Since Agisoft Metashape is not able to find many matches, it is critical to maximise the number of GCPs on all images. With this approach, we were able to obtain an orientation for our two images of interest with a re-projection error around 0.4 pixels.

After applying the previously estimated camera orientation and georeferencing the model, the tie points are compared with the DEM of the water surface. The mean elevation difference is -6 mm, the median is -8 mm and the standard deviation is 53 mm. The histogram of these differences is

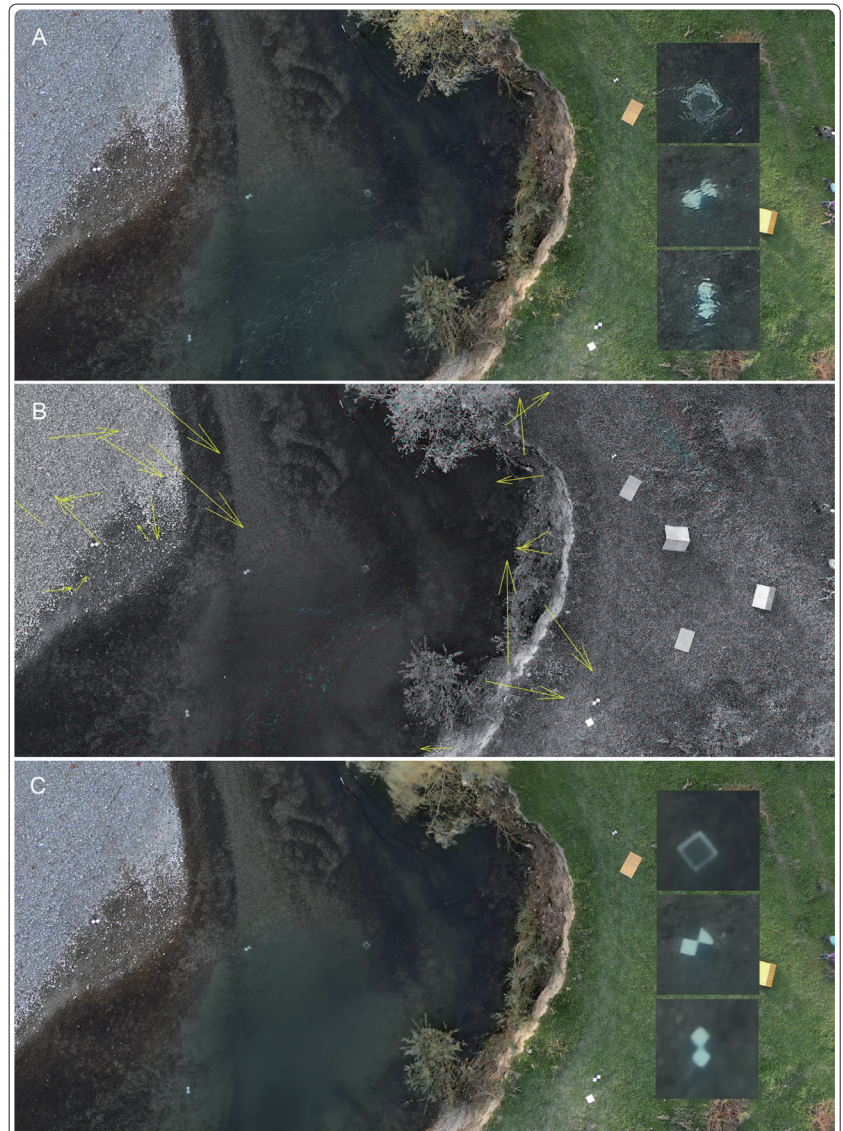


Fig. 10: Results obtained from image sequence processing. (A) Example image of a sequence (approximately 100 images) captured from one position. (B) Colour composite (overlay) of reference (red) and moving image (cyan). Arrows indicate residuals between reference and fitted tie points after co-registration (RMSE 0.11/0.10 pixel in x/y). (C) Corrected image with the geometry of an image which would have been taken through a calm flat water surface. Small image inlets illustrate the de-blurring effect at the checkerboard targets in detail

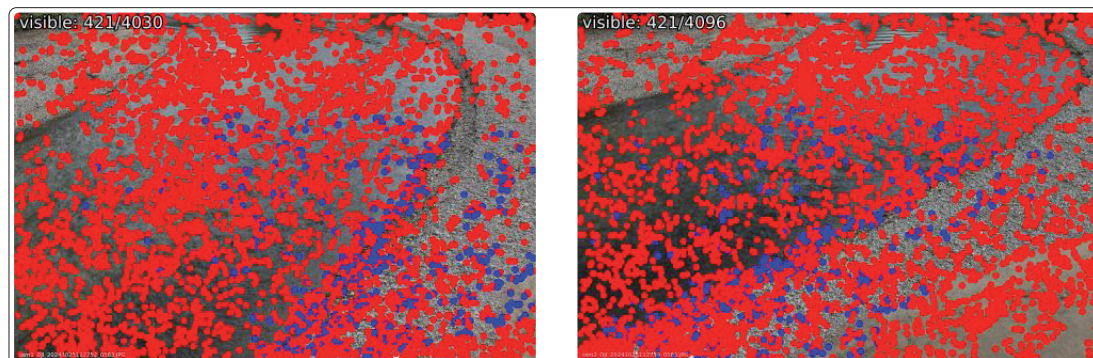


Fig. 11: Results from the feature detection and matching (by Superpoint and LightGlue). Each point is a detected feature and the blue points are the matches between both images

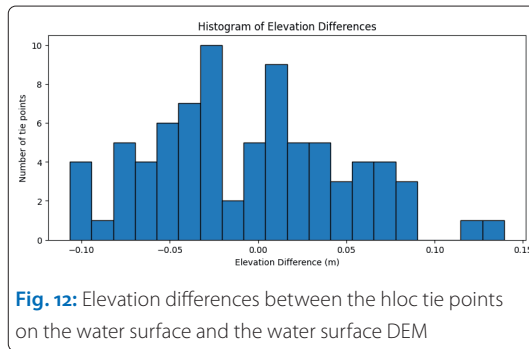


Fig. 12: Elevation differences between the hloc tie points on the water surface and the water surface DEM

Acknowledgments

The research presented was carried out within the transnational WEAVE projects PhotoBathyWave and BathyNeRF funded by the Austrian Science Fund (FWF) and the German Research Foundation (DFG). PhotobathyWave: I 5935-N (FWF), 496002628 (DFG); BathyNeRF: PIN1353223 (FWF), JU 2847/2-1(DFG).

presented in Fig. 12. Most tie points are within a distance of 10 cm from the water surface, below or above. They were estimated from images of a dynamic surface, which partly explains why the values are dispersed around the mean level of the water surface.

4.5 Topography and bathymetry from NeRFs

The results obtained from the Neural Radiance Field trained with the nadir and oblique images introduced in Section 2.2 are displayed in Fig. 13. The right side (B) shows a synthetic view of the Pielach dataset rendered from the NeRF inside the Nerfstudio viewer. The current implementation of the Nerfacto-Huge model assumes a straight image rays when training and rendering the NeRF. This means that beam refraction at the water-air interface is not considered so far, neither for training nor for view synthesis. This leads to a sub-optimal representation of the riverbed topography. This, in turn, affects the resulting 3D point cloud exported from Nerfstudio. The underwater points are sparse and noisy, and no clear river bottom can be mapped. In future work, we will first train the NeRF model considering simple and then more complex water surfaces as outlined in Section 3.5.

5 Conclusions

In this article, we introduced a benchmark dataset for mapping a riffle-pool-type pre-alpine gravel bed river with optical bathymetry. The Pielach River has been repeatedly captured for more than a decade with images and laser scans from crewed or uncrewed aerial platforms. Following a devas-

tating 300-year flood event in September 2024 (Bloeschl 2024), we surveyed a 750 m long section of the river with multicopter drones on October 24 to 25, 2024.

We first established a precise geodetic network based on GNSS and total station measurements, measured ground control points and saddle-roof shaped reference surfaces on land for precise georeferencing of the acquired airborne data. Our reference measurements also included a total station survey of 13 photogrammetric underwater targets and 19 river cross-sections.

The airborne survey consisted of a flight block with nadir and oblique images from a flying altitude of 80 m AGL. In addition, we also conducted experiments with a UAV hovering over certain waypoints taking sequences of 100 images before moving to the next position. In a separate experiment, we employed two UAVs and took synchronous oblique images of the water surface. The prior experiment was intended to mitigate the effects of the undulating water surface for precise bathymetry estimation with stereo images, and the latter experiment aimed to test the possibility of capturing the 3D shape of the instantaneous water surface as a prerequisite step for later integrated estimation of both water surface and bottom from synchronised UAV images. For all image acquisitions, we employed DJI M350 RTK multicopter UAVs equipped with DJI Zenmuse P1 RGB cameras. With this setup, we obtained a ground sampling distance of 1 cm at a flying altitude of 80 m.

The airborne data acquisition was complemented by topographic and topo-bathymetric flight missions. The prior served as a basis for capturing the river surroundings, including the alluvial forest enclosed by the mapped meander of the Pielach River, and for obtaining a precise model of the water surface needed for refraction correction. However, the main survey was the topo-bathymetric UAV flight with the RIEGL VQ-840-GL sensor. Due to the clear water, we were able to fully penetrate the entire river, including approximately 3 m deep pools. The final georeferenced and refraction-corrected 3D LiDAR point cloud provides a trustworthy areal reference for various photo bathymetry

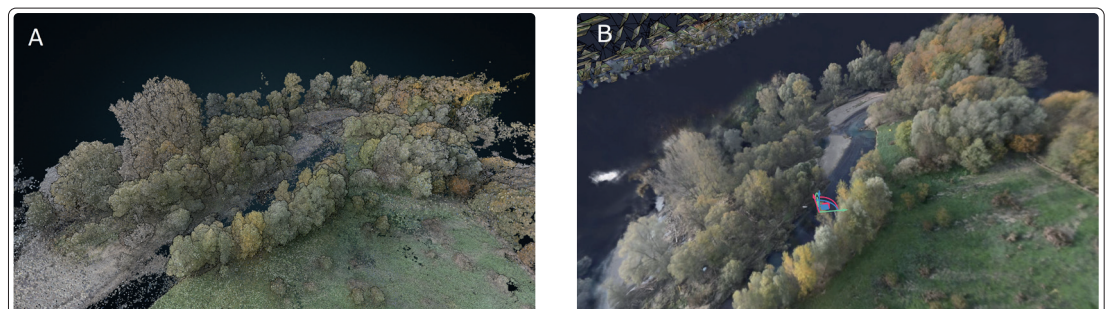


Fig. 13: Results from NeRF processing. (A) RGB-coloured 3D point cloud exported from Nerfstudio. (B) Synthetic view rendered from the trained NeRF

applications. Compared to the ground truth obtained from the total station measurements, the residual vertical errors of the bathymetric point cloud are less than 2 cm.

Next to the standard data processing, we also introduced novel and innovative approaches for mapping bathymetry and undulating water sur-

faces in 3D. This was made possible by applying image sequences instead of single image frames and by synchronous acquisition of oblique stereo images. As further novelty, we introduced our first ideas for using Neural Radiance Fields for bathymetry estimation. In future work, we will extend the presented research directions. //

Dataset

The dataset described in this article is available as open research data (DOI: 10.48436/taz19-r6618).

References

- Bloeschl, Günter (2024): September 2024 flooding in Central Europe: The Austrian experience. EGU Blogs, GeoLog, <https://blogs.egu.eu/geolog/2024/09/26/september-2024-flooding-in-central-europe-the-austrian-experience>
- Bryant, F. (1958): Snell's law of refraction. Physics Bulletin, DOI: 10.1088/0031-9112/9/12/004
- DeTone, Daniel; Tomasz Malisiewicz; Andrew Rabinovich (2018): Superpoint: Self-supervised interest point detection and description. Computer Vision and Pattern Recognition, DOI: 10.48550/arXiv:1712.07629
- Förstner, Werner; Bernhard P. Wrobel (2016): Photogrammetric Computer Vision: Statistics, Geometry, Orientation and Reconstruction. Springer International Publishing, DOI: 10.1007/978-3-319-11550-4
- Gkiatas, Georgios T.; Panagiotis D. Koutalakis; Ioannis K. Kasapidis; Vasilis Iakovoglou; Georios N. Zaimis (2022): Monitoring and quantifying the fluvio-geomorphological changes in a torrent channel using images from unmanned aerial vehicles. Hydrology, DOI: 10.3390/hydrology9100184
- Gira, Philipp; Norbert Pfeifer; Gottfried Mandlbürger (2016): Rigorous Strip Adjustment of UAV-based Laserscanning Data Including Time-Dependent Correction of Trajectory Errors. Photogrammetric Engineering & Remote Sensing, DOI: 10.14358/PERS.82.12.945
- Gueguen, Laure-Anne; Gottfried Mandlbürger (2024): Lab experiment for photo bathymetry. Hydrographische Nachrichten, DOI: 10.23784/HN129-06
- Guenther, Gary C.; A. Grant Cunningham; Paul E. LaRoque; David J. Reid (2000): Meeting the accuracy challenge in airborne lidar bathymetry. Proceedings of the 20th EARSeL Symposium: Workshop on Lidar Remote Sensing of Land and Sea, Dresden
- Hauer, Christoph; Gottfried Mandlbürger; Helmut Habersack (2009): Hydraulically related hydro-morphological units: description based on a new conceptual mesohabitat evaluation model (mem) using lidar data as geometric input. River Research and Applications, DOI: 10.1002/rra.1083
- Hirschmüller, Heiko (2008): Stereo Processing by Semiglobal Matching and Mutual Information. IEEE Transactions on Pattern Analysis and Machine Intelligence, DOI: 10.1109/TPAMI.2007.1166
- IHO (2008): S-44, Standards for Hydrographic Surveys. Standard 5th ed., International Hydrographic Organization, Monaco
- Kramer Stajnko, Janja; Renata Jecl; Matjaž Nekrep Perc (2023): Advances in monitoring and understanding the dynamics of suspended-sediment transport in the river drava, slovenia: An analysis more than a decade-long. Applied Sciences, DOI: 10.3390/app13159036
- Kraus, Karl (2007). Photogrammetry – Geometry from Images and Laser Scans. De Gruyter, DOI: 10.1515/9783110892871
- Lindenberger, Philipp; Paul-Edouard Sarlin; Marc Pollefeys (2023): Lightglue: Local feature matching at light speed. Computer Vision and Pattern Recognition, DOI: 10.48550/arXiv.2306.13643
- Lurton, Xavier (2002): An Introduction to Underwater Acoustics: Principles and Applications. Geophysical Sciences Series. Springer
- Maas, Hans-Gerd (2015): On the Accuracy Potential in Underwater/Multimedia Photogrammetry. Sensors, DOI: 10.3390/s150818140
- Mandlbürger, Gottfried (2019): Through-water dense image matching for shallow water bathymetry. Photogrammetric Engineering and Remote Sensing, DOI: 10.14358/pers.85.6.445
- Mandlbürger, Gottfried; Christoph Hauer; Martin Wieser; Norbert Pfeifer (2015): Topo-bathymetric LiDAR for monitoring river morphodynamics and instream habitats – A case study at the Pielach River. Remote Sensing, DOI: 10.3390/rs70506160
- Melcher, Andreas; Stefan Schmutz (2010): The importance of structural features for spawning habitat of nase *Chondrostoma nasus* (L.) and barbel *Barbus barbus* (L.) in a pre-alpine river. River Systems, DOI: 10.1127/1868-5749/2010/019-0033
- Mildenhall, Ben; Pratul P. Srinivasan; Matthew Tancik; Jonathan T. Barron; Ravi Ramamoorthi; Ren Ng (2021): NeRF: Representing scenes as neural radiance fields for view synthesis. Computer Vision and Pattern Recognition, DOI: 10.48550/arXiv.2003.08934
- Mulsow, Christian (2010): A flexible multi-media bundle approach. The International Archives of the Photogrammetry, Remote Sensing and Spatial Information Sciences
- Mulsow, Christian (2018): Digital elevation models of underwater structures from UAV imagery. Hydrographische Nachrichten, DOI: 10.23784/HN110-02
- Mulsow, Christian; Hannes Sardemann; Laure-Anne Gueguen; Gottfried Mandlbürger; Hans-Gerd Maas (2024): Concepts for compensation of wave effects when measuring through water surfaces in photogrammetric applications. The International Archives of the Photogrammetry, Remote Sensing and Spatial Information Sciences, DOI: 10.5194/isprs-archives-XLVIII-2-2024-289-2024

- Naura, Marc; Mike J. Clark; David A. Sear et al. (2016): Mapping habitat indices across river networks using spatial statistical modelling of river habitat survey data. *Ecological Indicators*, DOI: <https://doi.org/10.1016/j.ecolind.2016.01.019>
- Pfeifer, Norbert; Gottfried Mandlbürger; Johannes Otepka; Wilfried Karel (2014): OPALS – A framework for Airborne Laser Scanning data analysis. *Computers, Environment and Urban Systems*, DOI: [10.1016/j.compenvurbsys.2013.11.002](https://doi.org/10.1016/j.compenvurbsys.2013.11.002)
- Pfennigbauer, Martin; Clifford Wolf; Josef Weinkopf; Andres Ullrich (2014): Online waveform processing for demanding target situations. *SPIE Digital Library, Online Proceedings*, DOI: [10.1117/12.2052994](https://doi.org/10.1117/12.2052994)
- Philpot, William (Ed.) (2019). *Airborne Laser Hydrography II*. Cornell University Library, <https://hdl.handle.net/1813/58722>
- Pöpl, Florian; Andreas Ullrich; Gottfried Mandlbürger; Norbert Pfeifer (2024): A flexible trajectory estimation methodology for kinematic laser scanning. *ISPRS Journal of Photogrammetry and Remote Sensing*, DOI: [10.1016/j.isprsjprs.2024.06.014](https://doi.org/10.1016/j.isprsjprs.2024.06.014)
- Rhomberg-Kauert, Jan; Lucas Dammert; Michael Groemer; Martin Pfennigbauer; Gottfried Mandlbürger (2024): Macrophyte detection with bathymetric LiDAR – Applications of high-dimensional data analysis for submerged ecosystems. *The International Hydrographic Review*, DOI: [10.58440/ihr-30-2-a16](https://doi.org/10.58440/ihr-30-2-a16)
- Sardemann, Hannes; Christian Mulsow; Laure-Anne Gueguen; Gottfried Mandlbürger; Hans-Gerd Maas (2024): Multimedia photogrammetry with non-planar water surfaces – accuracy analysis on simulation basis. *The International Archives of the Photogrammetry, Remote Sensing and Spatial Information Sciences*, DOI: [10.5194/isprs-archives-XLVIII-2-2024-363-2024](https://doi.org/10.5194/isprs-archives-XLVIII-2-2024-363-2024)
- Sarlin, Paul-Edouard; Cesar Cadena; Roland Siegwart; Marcin Dymczyk (2019): From coarse to fine: Robust hierarchical localization at large scale. *Computer Vision and Pattern Recognition*, DOI: [10.48550/arXiv.1812.03506](https://doi.org/10.48550/arXiv.1812.03506)
- Schwarz, Roland; Gottfried Mandlbürger; Martin Pfennigbauer; Norbert Pfeifer (2019): Design and evaluation of a full-wave surface and bottom-detection algorithm for LiDAR bathymetry of very shallow waters. *ISPRS Journal of Photogrammetry and Remote Sensing*, DOI: [10.1016/j.isprsjprs.2019.02.002](https://doi.org/10.1016/j.isprsjprs.2019.02.002)
- Schwarz, Roland; Norbert Pfeifer; Martin Pfennigbauer; Andreas Ullrich (2017): Exponential Decomposition with Implicit Deconvolution of Lidar Backscatter from the Water Column. *PFG – Journal of Photogrammetry, Remote Sensing and Geoinformation Science*, DOI: [10.1007/s41064-017-0018-z](https://doi.org/10.1007/s41064-017-0018-z)
- Tsakiris, George (2014): Flood risk assessment: concepts, modelling, applications. *Natural Hazards and Earth System Sciences*, DOI: [10.5194/nhess-14-1361-2014](https://doi.org/10.5194/nhess-14-1361-2014)
- Wagner, Nike; Gunnar Franke; Klaus Schmieder; Gottfried Mandlbürger (2024): Automatic classification of submerged macrophytes at Lake Constance using laser bathymetry point clouds. *Remote Sensing*, DOI: [10.3390/rs16132257](https://doi.org/10.3390/rs16132257)
- Wenzel, Konrad; Mathias Rothermel; Norbert Haala; Dieter Fritsch (2013): SURE – The ifp Software for Dense Image Matching. In: Dieter Fritsch (Editor): *Photogrammetric Week '13*, Wichmann/VDE Verlag, pages 59–70
- Westfeld, Patrick; Hans-Gerd Maas; Katja Richter; Robert Weiß (2017): Analysis and correction of ocean wave pattern induced systematic coordinate errors in airborne LiDAR bathymetry. *ISPRS Journal of Photogrammetry and Remote Sensing*, DOI: [10.1016/j.isprsjprs.2017.04.008](https://doi.org/10.1016/j.isprsjprs.2017.04.008)
- Zigann, Julia Marie; Richard M. Gersberg; Volker Lüderitz (2023): Effects of deadwood on macroinvertebrate assemblages in three sand-type lowland streams. *Ecologies*, DOI: [10.3390/ecologies4010008](https://doi.org/10.3390/ecologies4010008)
- Zitek, Andreas; Stefan Schmutz; Matthias Jungwirth (2008): Assessing the efficiency of connectivity measures with regard to the EU-Water Framework Directive in a Danube-tributary system. *Hydrobiologia*, DOI: [10.1007/s10750-008-9394-0](https://doi.org/10.1007/s10750-008-9394-0)